MATERIALS SCIENCE

Snoek-type damping performance in strong and ductile high-entropy alloys

Zhifeng Lei[1,2], Yuan Wu[1]*, Junyang He[2], Xiongjun Liu[1], Hui Wang[1], Suihe Jiang[1], Lin Gu[3], Qinghua Zhang[3], Baptiste Gault[2,4], Dierk Raabe[2], Zhaoping Lu[1]*

Noise and mechanical vibrations not only cause damage to devices, but also present major public health hazards. High-damping alloys that eliminate noise and mechanical vibrations are therefore required. Yet, low operating temperatures and insufficient strength/ductility ratios in currently available high-damping alloys limit their applicability. Using the concept of high-entropy alloy (HEA), we present a class of high-damping materials. The design is based on refractory HEAs, solid-solutions doped with either 2.0 atomic % oxygen or nitrogen, $(Ta0.5Nb0.5HfZrTi)_{98}O_2$ and $(Ta0.5Nb0.5HfZrTi)_{98}N_2$. Via Snoek relaxation and ordered interstitial complexes mediated strain hardening, the damping capacity of these HEAs is as high as 0.030, and the damping peak reaches up to 800 K. The model HEAs also exhibit a high tensile yield strength of ~1400 MPa combined with a large ductility of ~20%. The high-temperature damping properties, together with superb mechanical properties make these HEAs attractive for applications where noise and vibrations must be reduced.

INTRODUCTION

High-damping alloys are an important family of metallic materials for applications that require noise/vibration reduction, shock absorption, and energy conversion, in structures ranging from large-scale aircrafts to small-sized electrical devices (*1*). Traditional alloys used to reduce noise and vibrations achieve their mechanical damping capacity by primarily manipulating crystalline defects or/and interfaces, such as dislocations (*2*, *3*), phase or twin boundaries (*4*–*6*), and magnetic domain boundaries (*7*). However, when exposed to mechanical vibrations and the associated stresses, both crystal defects and interfaces in these conventional alloys tend to rearrange and aggregate. As a result, the whole relaxation process is irreversible and the damping capacity gradually deteriorates (*1*, *8*). In addition, these irreversible relaxation processes accelerate when the service temperature increases. This means that structural stability and the high-temperature damping capacity of traditional noise reduction alloys are often insufficient for long-term use (*8*, *9*). Moreover, those internal structural features that create high damping ability (mobile defects) scale inversely with mechanisms that lead to good mechanical strength (immobile defects). Therefore, in traditional high-damping alloy design concepts, high damping and high strength/ductility are often mutually exclusive (*10*).

Snoek relaxation, proposed in 1941 (*11*), is suited for equipping materials with damping properties and maintains those over long-term exposure to vibrations. Several bcc (body-centered cubic) systems show Snoek-type damping behavior, where the mechanical energy loss originates from the stress-induced ordering of interstitials (*12*, *13*). However, these Snoek-type high-damping alloys generally showed insufficient strength and ductility for mechanically highly demanding application scenarios. Recently, a family of metallic materials was proposed where multiple principal elements are in equimolar or near equimolar ratios to maximize the configurational entropy, hence termed high-entropy alloys (HEAs) (*14*, *15*). In HEAs, the difference in atomic sizes and chemistry among the multiple constituents lead to large lattice distortion (*16*) and sluggish atomic diffusion (*17*). The intrinsically highly distorted lattices of these materials increase solubility for interstitial atoms, which, in turn, can substantially impede dislocation movement (*18*–*20*). The high configurational entropy in these alloys stabilizes solid-solution phases, particularly at elevated temperatures (*21*). Recent experimental investigations have shown that the strength and ductility of typical bcc HEAs could be simultaneously enhanced by the addition of interstitial atoms. Ordered interstitial complexes–mediated strain hardening contributes to the improved mechanical performance (*22*).

Here, we report about a previously undiscovered class of high-damping alloys that are both mechanically strong and workable at high temperatures. The current alloy design concept has been realized in the form of a set of model Ta0.5Nb0.5HfZrTi HEAs blended with 2.0 atomic % (at %) oxygen or nitrogen, respectively. These high-damping HEAs show a good combination of high-temperature damping capacity, i.e., their peak damping capacity is as high as ~0.030 at a peak temperature of nearly 800 K, along with excellent mechanical properties (tensile yield strength, ~1400 MPa; elongation, ~20%). The findings not only introduce a class of high-damping materials for engineering applications but also shed light on understanding the mechanisms of mechanical damping in general and specifically at elevated temperatures.

RESULTS

Chemical analysis

The bcc HEAs, comprising group IV (Ti, Zr, Hf) and V (V, Nb, Ta) refractory elements, exhibit superior mechanical properties (*22*–*26*). These materials are attractive for optimizing damping response because their constituents have high solubility of both oxygen and nitrogen (>5.0 at %) (*27*). Here, we report results on the model HEA

[1]Beijing Advanced Innovation Center for Materials Genome Engineering, State Key Laboratory for Advanced Metals and Materials, University of Science and Technology Beijing, Beijing 100083, China. [2]Department of Microstructure Physics and Alloy Design, Max-Planck-Institut für Eisenforschung, Düsseldorf, Germany. [3]Beijing National Laboratory for Condensed Matter Physics, Institute of Physics, Chinese Academy of Sciences, Beijing 100190, China. [4]Department of Materials, Royal School of Mines, Imperial College, Prince Consort Road, London SW7 2BP, UK.
*Corresponding author. Email: luzp@ustb.edu.cn (Z.Lu); wuyuan@ustb.edu.cn (Y.W.)

Ta0.5Nb0.5HfZrTi (hereafter denoted as the base HEA), an oxygen-doped variant $(Ta0.5Nb0.5HfZrTi)_{98}O_2$ (hereafter denoted as O-2 HEA), and a nitrogen-doped variant $(Ta0.5Nb0.5HfZrTi)_{98}N_2$ (hereafter referred to as N-2 HEA). Table S1 presents the inert gas fusion analysis results of oxygen and nitrogen in the as-cast refractory HEAs. The actual impurity concentrations are very close to the target, indicating that the addition of TiO_2 and TiN as a resource of oxygen and nitrogen is reliable in this study. It should be noted that even in the base HEA, the level of oxygen is 0.377 at %, resulting from the fabrication process.

Damping properties

The damping capacity tanδ is a measure of the energy dissipation in a material and can be calculated as the ratio of the loss modulus E'' to the storage modulus E' (*28*). Moreover, the peak capacity of damping $\tan\delta_{max}$, determined by using a multifunction internal friction instrument, delineates the maximum energy dissipation during damping of a material. A higher $\tan\delta_{max}$ indicates larger energy dissipation, and high-damping alloys are metallic materials with $\tan\delta_{max} > 0.01$ (*28*). Figure 1 (A to C) illustrates the temperature-dependent variation of damping capacity tanδ of the three HEAs. The current HEAs exhibit good damping features with $\tan\delta_{max} > 0.01$. Specifically at 1.0 Hz, the $\tan\delta_{max}$ of the reference HEA Ta0.5Nb0.5HfZrTi reaches a high damping value of 0.014. The addition of oxygen or nitrogen effectively further enhances the damping capacity, and the $\tan\delta_{max}$ value at 1.0 Hz of the O-2 and N-2 HEAs increases to 0.020 and 0.027, respectively. The data also reveal that the relaxation peaks are thermally activated since the peak temperature increases while the peak height (i.e., $\tan\delta_{max}$) decreases with increasing vibration frequency. Such a frequency-dependent damping behavior is characteristic of strain relaxation damping, i.e., Snoek damping (*29*). This suggests that the current HEAs are Snoek-type high-damping alloys in which the stress-induced position switch of interstitial atoms gives rise to the corresponding internal friction peaks (*11*). It should be noted that the Snoek-type relaxation is intrinsically amplitude-independent. Yet, the here observed damping response seems to lead to a more complex interstitial relaxation response with a higher variety of possible interstitial site switches. This effect leads to a Snoek signal in the current HEAs where the relaxation peaks are much broader than a Debye peak. This observation shows that the high variety of local atomic configurations in these complex solid-solution alloys has a substantial effect on the variety of the resulting thermally activated site switching events. The base HEA used as reference material also shows a Snoek-type damping behavior, which might be due to the trace oxygen contamination from the fabrication process, as confirmed by the data shown in table S1. Moreover, in addition to a main damping peak at high temperature, a distinct additional damping peak at low temperature (see white arrows in Fig. 1, B and C) was observed in the O-2 and N-2 HEAs. The different internal friction peaks correspond to different mechanisms behind the underlying atomic relaxation steps of the interstitials. Thus, the occurrence of additional peaks indicates the presence of different types of stress-induced reorientation processes (*29*).

According to the anelastic nature of the Snoek-type strain relaxation process (*29*), the activation energy H is proportional to the peak temperature T_p. For interstitial atoms in a host bcc lattice, the activation of the corresponding stress-induced reorientation process determines the peak temperature T_p. To obtain the activation energy H associated with specific stress-induced reorientation mechanisms of the interstitial atoms, we conducted an Arrhenius analysis (*30*)

$$\ln 2\pi f + \ln \tau_0 + \left(\frac{H}{k_B}\right) T_p^{-1} = 0 \quad (1)$$

as shown in Fig. 1D. Here, f is the vibration or excitation frequency, τ_0 is the relaxation time at infinite temperature for the strain relaxation process, and k_B is the Boltzmann constant. The activation energy H is estimated to be 2.06, 2.40, and 4.06 eV for the reference alloy and the interstitially doped O-2 and N-2 HEAs, respectively. The activation energy H of the N-2 HEA is much higher than that of the base and O-2 HEA, implying that the nitrogen atoms switch their positions at higher barriers than oxygen in the Ta0.5Nb0.5HfZrTi HEA matrix.

Comparison of the damping properties

To demonstrate the effectiveness of the entropy-stabilization alloy design concept, a comparison of the damping properties was conducted. Figure 2A shows the peak temperature T_p and the activation energy H of the current HEAs compared with those of conventional Snoek-type damping alloys (*11*, *12*, *31*–*42*). Both, T_p and H of the current HEAs are much higher than those of interstitially doped conventional alloys. In addition to the peak capacity of damping $\tan\delta_{max}$, the width of the damping peak ΔT and the peak temperature T_p are also important parameters for a material's damping capability. ΔT determines the damping operating temperature range, and T_p permits the upper temperature limit for damping applications. According to the Debye expression for a single relaxation process, ΔT, which describes the separation of the two temperatures corresponding to the half-height of $\tan\delta_{max}$, can be expressed as $\Delta T = 2.63 k_B T_p^2 / H$ (*12*). Figure 2B reveals a three-dimensional diagram of $\tan\delta_{max}$-ΔT-T_p of the studied HEAs, in comparison with traditional Snoek-type damping alloys (*11*, *12*, *31*–*42*). The analysis shows that the current high-entropy damping alloys can be used at a much higher temperature (737, 747, and 730 K for the base, O-2, and N-2 HEAs at 1.0 Hz, respectively.) and wider operating temperature range (60, 53, and 30 K for the base, O-2, and N-2 HEAs at 1.0 Hz, respectively.) than any other damping material reported so far, including Cu-, Mg-, and Fe-based alloys.

Mechanical properties

To enable practical applications, high-damping alloys combined with good quasi-static mechanical properties such as strength and damage tolerance can provide attractive engineering and economic solutions to problems involving seismic, shock, and vibration isolation. Figure 3A shows the true tensile stress-strain curves of the current HEAs. The base HEA, used here as reference material, shows a yield strength of ~810 MPa at an elongation of ~10.8%, which is superior to that of other Ti-Nb alloys reported to date (*43*). The interstitial doped HEAs have a strong solid-solution strengthening, i.e., the yield strength was increased to 1138 and 1362 MPa for the O-2 and N-2 HEAs, respectively. Interstitial reinforcement by nitrogen is more effective than that conveyed by oxygen doping. The addition of either oxygen or nitrogen to the base HEA did not appreciably deteriorate the work hardening behavior. Particularly, the ductility of the O-2 HEA was unexpectedly doubled, which has been earlier associated with the formation of ordered interstitial

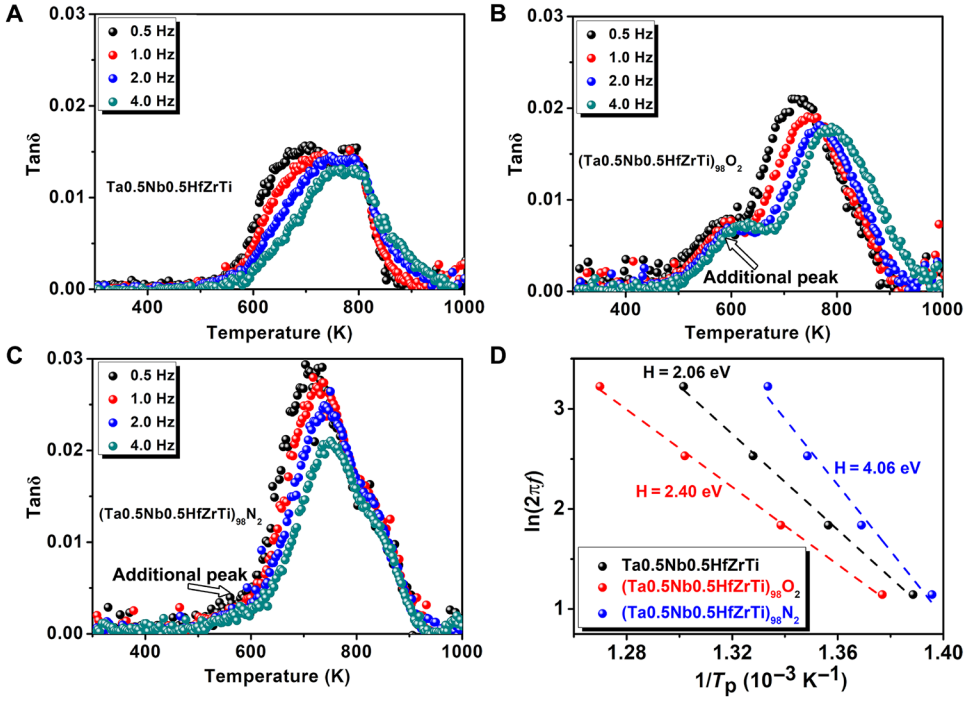

Fig. 1. Damping properties of the oxygen- or nitrogen-doped Ta0.5Nb0.5HfZrTi HEAs. Temperature-dependent variation of damping capacity (indexed by tanδ) of the as-cast (**A**) Ta0.5Nb0.5HfZrTi, (**B**) $(Ta0.5Nb0.5HfZrTi)_{98}O_2$, and (**C**) $(Ta0.5Nb0.5HfZrTi)_{98}N_2$ HEAs. The measurements were conducted on a multifunction internal friction apparatus by the forced vibration at 0.5, 1.0, 2.0, and 4.0 Hz, respectively. The maximum strain amplitude is 2×10^{-4}, and the heating rate is 2 K min^{-1} in the measured temperature range. The three HEAs present a promising high damping property with the peak capacity of damping $tan\delta_{max} > 0.01$. The white arrows in (B) and (C) indicate the additional low-temperature peak in the $(Ta0.5Nb0.5HfZrTi)_{98}O_2$ and $(Ta0.5Nb0.5HfZrTi)_{98}N_2$ HEAs, respectively. (**D**) Arrhenius plots of the Snoek damping peak of the current HEAs, and the slope of the linear variation of $ln(2\pi f)$ versus $1/T_p$ yields the activation energy H of the corresponding stress-induced reorientation process.

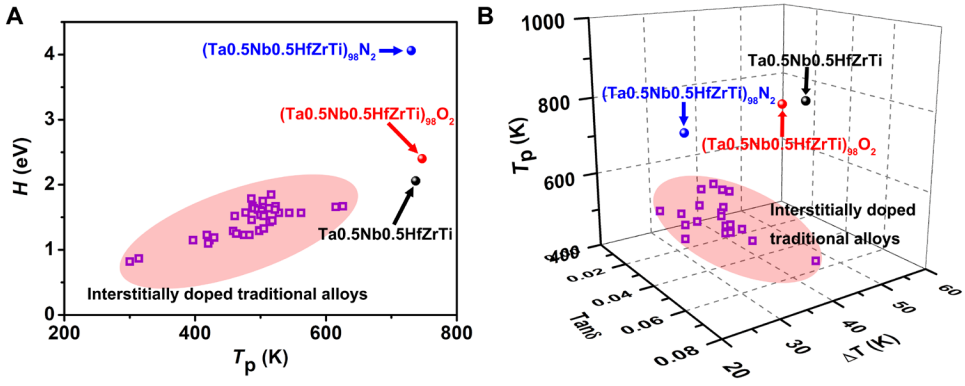

Fig. 2. A comparison of the damping properties of the model HEAs with the traditional Snoek-type damping alloys. (**A**) The damping peak temperature T_p and the corresponding activation energy H in the current HEAs and other conventional Snoek-type damping alloys (see squares). The T_p and H of the current HEAs are much higher than that of the traditional alloys. (**B**) Plot of the peak capacity of damping $tan\delta_{max}$, the width of the Snoek damping peak ΔT, and the peak temperature T_p. The data for the typical Snoek-type damping alloys are plotted for comparison. The current Snoek-type high-damping HEAs exhibit higher T_p and ΔT, which means that the designed HEAs can be used at a much higher temperature and a wider operating temperature range.

complexes that provide high strain hardening (*22*). In addition, the large ductility of the nitrogen-containing N-2 HEA is retained, which is attributed to the appearance of ordered nitrogen complexes that impede dislocation motion (see below). Compared with the Ti-25Nb-*x*O at % Snoek-type high-damping alloys (*12*), the overall mechanical properties of the interstitially alloyed HEAs are substantially enhanced. The interstitial doped HEAs retain the same level of ductility but display 70 to 105% higher yield strength than Ti-25Nb-1.5O alloy. Although the specific damping index and tensile strength of hydrogenated metallic glasses are comparable to those of the currently developed HEAs, their small dimensions (they are usually produced in small volumes as they require high quenching rates) and low thermal stability make them less suitable for damping applications for larger structures and at elevated temperatures (*44*–*48*).

Microstructures

To understand the origin of the high damping capacity and excellent mechanical properties, Fig. 4 shows the typical microstructure

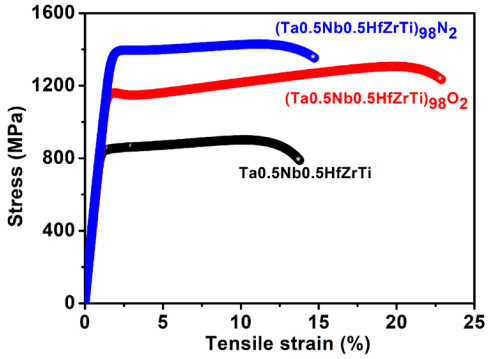

Fig. 3. Mechanical properties of the oxygen- or nitrogen-doped Ta0.5Nb0.5HfZrTi HEAs. Room temperature tensile stress-strain curves for the as-cast Ta0.5Nb0.5HfZrTi and its corresponding 2.0 at % oxygen- or nitrogen-dissolved HEAs. Adding interstitials leads to the simultaneous strengthening and ductilizing.

of the interstitially alloyed HEAs. X-ray diffraction (XRD) patterns demonstrate that both the base and interstitial doped HEAs have single-phase bcc structure (Fig. 4A). Electron backscatter diffraction (EBSD) reveals that the average grain size is similar for the base (76.7 μm), O-2 (70.0 μm), and N-2 (92.3 μm) alloys, and all the three materials show random crystallographic texture (Fig. 4, B to D). The atomic-scale structures of the alloys were characterized by aberration-corrected scanning transmission electron microscopy (STEM), and Fig. 4 (E to G) depicts typical results for material O-2 HEA. Figure 4E shows a high-angle annular dark-field (HAADF) micrograph with the incident electron beam aligned along the $[011]_{bcc}$ zone axis of the grain selected. The *Z*-contrast image is highly sensitive to local variations in the atomic number of the constituent elements in the illuminated atomic column (*49*), i.e., light atoms exhibit dark contrast while heavy atoms display bright contrast. The *Z*-contrast of the STEM-HAADF image reveals the existence of light-atom–enriched regions, viz., these zones are (Zr, Ti) rich, and heavy-atom–enriched regions, i.e., (Ta, Nb, Hf) rich (Fig. 4F). This means that compositional clusters of metallic elements in the O-2 HEA were formed, similar to what was reported previously (*22*). Similar zones were revealed by STEM imaging of the base and N-2 HEAs (see fig. S1), demonstrating that these clusters among the metallic matrix elements are intrinsic features in these bcc HEAs. The aberration-corrected STEM-ABF (annular bright field) image (Fig. 4G) reveals that oxygen occupies the interstitial sites in the bcc lattice (see the white arrows in Fig. 4G). Furthermore, statistical analysis of the STEM-HAADF and the corresponding ABF images (Fig. 4, F and G) confirm that oxygen tends to prefer interstitial positions adjacent to lattice sites, which are occupied by light atoms (i.e., Zr and/or Ti), accumulating to the so-called ordered oxygen complexes (*22*). Figure 4 (H and I) shows the atom probe tomography analysis of the O-2 HEA. In Fig. 4H, a set of cyan-colored isocomposition surfaces reveals regions containing more than 3.5 at % O, showing the presence of O-rich clusters, i.e., ordered oxygen complexes (*22*). Figure 4I presents the elemental partitioning behavior across the matrix/ordered oxygen complex interfaces. The composition profiles were analyzed as a function of the distance to the isocomposition surface. The slight enrichment of Zr and Ti atoms and the corresponding depletion of Ta, Nb, and Hf atoms were observed within the O-rich clusters. These observations are consistent with the ABF images provided by STEM probing of the O-2 HEA. This result further demonstrates the formation of ordered oxygen complexes. The appearance of an additional low-temperature damping peak in the O-2 material (see Fig. 1B) also indicates the existence of the ordered oxygen complexes (*22*). Unexpectedly, we also observed ordered nitrogen complexes in the N-2 material (see fig. S1), although at a much smaller frequency compared to the oxygen clusters observed in the O-2 alloy.

DISCUSSION

We observed that the relaxation peaks in the current HEAs are asymmetrically broadened (see Fig. 1, A to C). This is a feature associated with the variety of interstitial relaxation processes involved in these massive solid solutions (*28*). Because of the complexity in alloy composition and the resulting multitude in local chemical environments in which the interstitial atoms switch their positions, it is difficult to conduct a complete peak deconvolution analysis based on all possible individual relaxation processes. However, two main configurations of the interstitial atoms can indeed be distinguished in the current material, namely, position switches of interstitials in ordered interstitial complexes and relaxation of randomly distributed interstitial atoms (*22*). These two kinds of configurations both contribute to the current Snoek relaxation and can cause at least some of the asymmetries observed. Therefore, we conduct a decomposition of the relaxation structure in terms of the two main classes of interstitial configurations (see the Supplementary Materials). Figure 5 (A to C) shows the anelastic relaxation spectra (at 1.0 Hz) of the base Ta0.5Nb0.5HfZrTi, O-2 $(Ta0.5Nb0.5HfZrTi)_{98}O_2$, and N-2 $(Ta0.5Nb0.5HfZrTi)_{98}N_2$ HEAs as the sum of decomposed peaks. The fitting curves are in good agreement with the experimental data points, with a correlation index above 0.99. For the base HEA, two peaks could be resolved at 710 and 798 K, respectively (see green and magenta curves in Fig. 5A). As there is no ordered interstitial complex in the base HEA, the two decomposed peaks probably originate from the jumps of the randomly distributed interstitial atoms. These impurities come from the synthesis process and raw materials. Because of the complicated occupation of the Ta, Nb, Hf, Zr, and Ti elements in the current HEAs, it is difficult to determine the actual clusters attributing to these two peaks. The height of the two Snoek damping peaks is 0.014 and 0.006, respectively. In the material with 2.0 at % oxygen, i.e., in the O-2 HEA, a low-temperature peak (red curve in Fig. 5B) appears at 577 K, in addition to the two high-temperature peaks (green and magenta curves in Fig. 5B) that occur at 748 and 850 K, respectively. The formation of ordered oxygen complexes gives rise to the additional low-temperature peak (*22*), and the randomly distributed oxygen atoms produce the two high-temperature peaks. The height of the additional peak and of the two high-temperature peaks is 0.005, 0.020, and 0.002, respectively. The maximum peak height of the O-2 HEA (i.e., 0.020) is higher than that of the base HEA (i.e., 0.014). For a specific alloy system, the magnitude of the Snoek damping peak height follows a linear relationship with the solute element concentration (*28*, *29*). Therefore, the higher peak height of the O-2 HEA is due to its higher oxygen content, compared to the base HEA (see table S1). Moreover, as estimated by the ratio between the peak height of the additional peak and the total peak height, ~18.5% of all the oxygen atoms in the O-2 HEA participate in the formation of ordered oxygen complexes, enabling the enhanced ductility of this material (*22*). For the nitrogen-doped N-2 HEA, an additional low-temperature peak (blue curve)

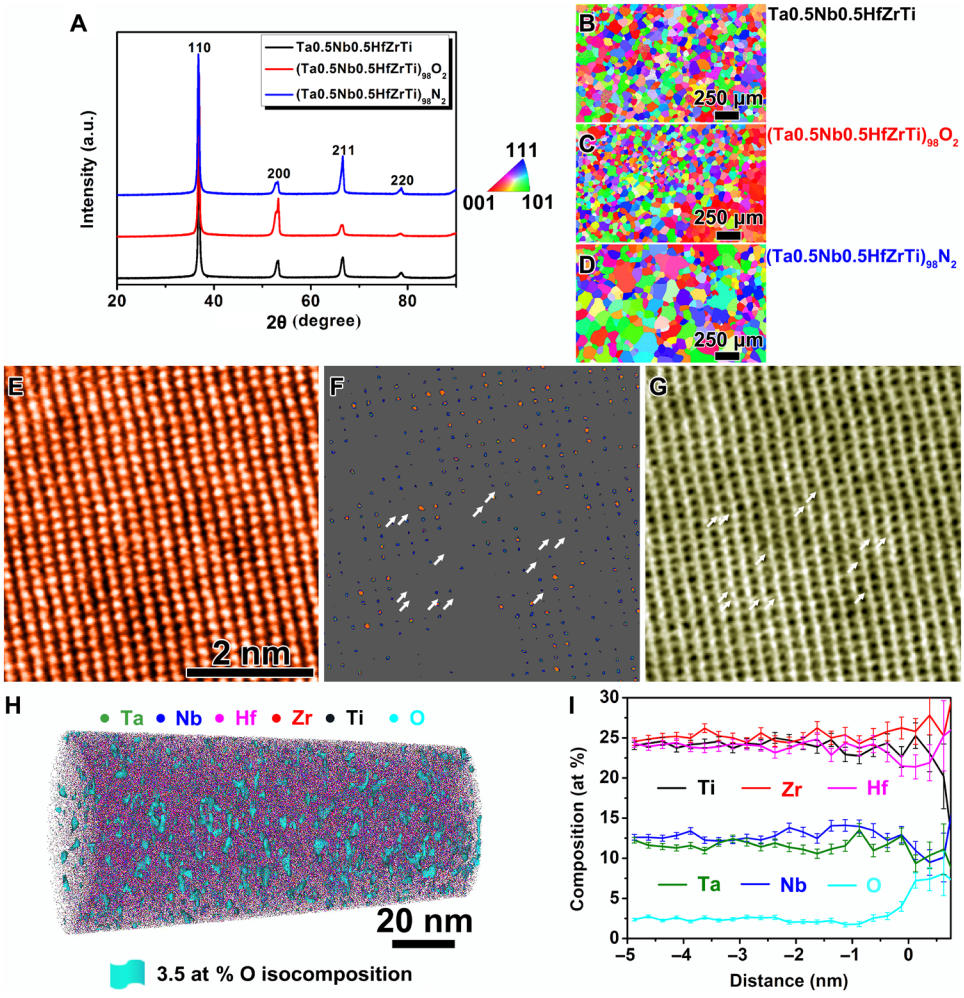

Fig. 4. Microstructure revolution of the oxygen- or nitrogen-doped Ta0.5Nb0.5HfZrTi HEAs. (**A**) XRD patterns of the as-cast HEAs and (**B** to **D**) the corresponding EBSD images. All the as-cast HEAs have single bcc lattice structure. (**E** to **G**) STEM-HAADF images for the $[011]_{bcc}$ crystal axis with differently adjusted contrast to reveal the existence of compositional clusters in the $(Ta0.5Nb0.5HfZrTi)_{98}O_2$ HEA and the corresponding STEM-ABF image to reveal the ordered oxygen complexes. The white arrows indicate the positions of the oxygen atom columns. (**H**) Atom probe tomography reconstruction from the analysis of a specimen from the $(Ta0.5Nb0.5HfZrTi)_{98}O_2$ HEA. The threshold for the isocomposition surface is 3.5 at % O, revealing the presence of ordered oxygen complexes. (**I**) Proxigram from the interface matrix/ordered oxygen complex showing the enrichment of O, Ti, Zr and slightly depletion of Ta, Nb, Hf. a.u., arbitrary units.

and two high-temperature peaks (green and magenta curves) were also observed (see Fig. 5C). The peak height of the additional low-temperature peak is 0.002, and that of the two high-temperature peaks is 0.027 and 0.009, respectively. Hence, only ~5.3% of all the nitrogen atoms in the N-2 HEA contribute to the formation of ordered nitrogen complexes. As most of the nitrogen is interstitially randomly distributed, the N-2 HEA shows the strongest damping peak among all three HEAs studied here. This analysis shows that ordered interstitial complexes contribute to the enhancement of ductility while randomly distributed interstitial atoms improve mechanical damping.

Figure 5D schematically illustrates the mechanism of developing HEAs with high damping capacity and good mechanical properties. The base HEA exhibits a relatively low yield strength (~810 MPa) and a small damping capacity (~0.014 at 1.0 Hz) due to its low interstitial alloying content (only ~0.377 at %). The addition of 2.0 at % oxygen enhances not only the yield strength to ~1138 MPa but also the maximum damping ability to ~0.020 at 1.0 Hz. The oxygen atoms (~18.5%) induce the formation of ordered interstitial complexes, which greatly benefit the plastic deformation and increase the ductility to ~20%. With the addition of 2.0 at % nitrogen, the larger atomic size of nitrogen (atomic radius of 0.75 Å) compared to that of oxygen (0.65 Å) leads to higher strengthening; thus, the yield strength of the N-2 HEA is ~224 MPa higher than that of the O-2 HEA. Moreover, ~94.7% of the nitrogen atoms are randomly distributed across the interstitial sites. As a result, the N-2 HEA exhibits both improved tensile yield strength (σ_y ~ 1362 MPa) and damping properties ($\tan\delta_{max}$ ~ 0.027 at 1.0 Hz). In addition, the ductility of the N-2 HEA (~11.9%) was not obviously deteriorated because of the formation of the limited ordered nitrogen complexes, in comparison to the base HEA.

It is also important to note that the peak temperature of damping in the current Snoek-type high-damping HEAs is approximately 100 K higher than that in traditional high-damping alloys

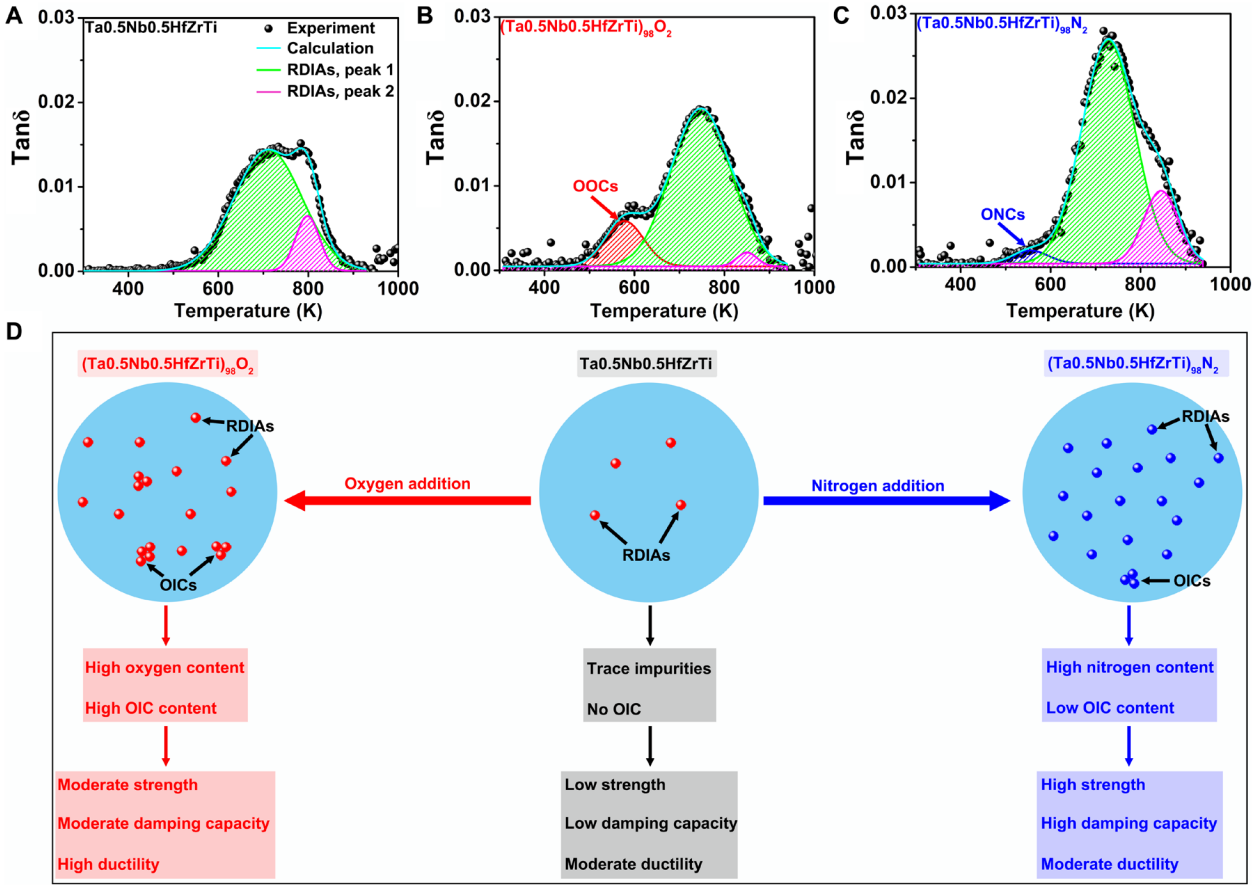

Fig. 5. Mechanism analysis of the strong and ductile high-damping HEAs. Temperature dependence of internal friction (at 1.0 Hz) and the fitting results in the (**A**) Ta0.5Nb0.5HfZrTi, (**B**) $(Ta0.5Nb0.5HfZrTi)_{98}O_2$, and (**C**) $(Ta0.5Nb0.5HfZrTi)_{98}N_2$ HEAs. The filled black circles are the experimental points, and the cyan curves are the sum of the cumulative fitting peaks. The green and magenta curves correspond to the relaxation process, which are due to the stress-induced ordering of the randomly distributed interstitial atoms (RDIAs). The red curve in (B) and the blue curve in (C) indicate the reorientation of ordered oxygen complexes (OOCs) and ordered nitrogen complexes (ONCs), respectively. The fitting correlation index is more than 0.99. (**D**) Schematic diagram of designing Snoek-type high-damping HEAs with high damping capacities and superb mechanical properties. OICs, ordered interstitial complexes. Interstitial strengthening contributes to the high strength, a sufficient concentration of randomly distributed interstitial atoms favors the enhancement of damping capacity, and an abundant OIC serves to improve the ductility.

(*11*, *12*, *31*–*42*). Because of the high configuration entropy and severely distorted lattices of HEAs (*50*), atomic position switches of interstitials in these matrices are impeded by the high atomic-scale distortion fields (*51*). This effect gives rise to the high activation temperatures and barrier energies for the interstitial reorientation steps and the resulting high-temperature damping capability. Moreover, the current alloy design strategy could be used to develop other high-damping HEAs as well (see fig. S2).

One has to note that the main structural features responsible for the high mechanical damping capacity of some of the established high-damping reference materials are highly heterogeneous microstructures, thermoelastic martensite, magnetic domains, or easily moveable dislocations, which generally show an amplitude dependence of damping (*52*). However, the high damping capacity of the alloy class discussed here is amplitude independent and originates instead from the high configurational variety of the underlying interstitial relaxation processes characteristic for compositionally complex solid-solution alloys. This mechanism leads to strongly broadened Snoek-type peaks. Similar to the hydrogen-containing high-damping alloys reported previously (*53*), the here discussed high interstitial refractory HEAs may be regarded as a kind of high-damping alloys. Potential applications of these high-damping alloys could be found in the automotive and aerospace industries.

In summary, via an entropy stabilization concept, we develop a class of Snoek-type high-temperature, high-damping alloys with additions of either oxygen or nitrogen atoms. These interstitial atoms in the severely distorted matrices with complex chemical short-range orders result in high strengthening, large ductility, and good high-temperature damping properties. The yield strength of the current HEAs (1138 and 1362 MPa for the O-2 and N-2 HEAs, respectively.) is much higher than that of the traditional high-damping alloys (~200 to 600 MPa) and twice that of the Ti-25Nb-1.5O Snoek-type high-damping alloy (~665 MPa). The here designed HEAs also have large tensile ductility (~20%). In addition, the peak capacity of damping is as high as 0.030 for the N-2 HEA at 0.5 Hz, which corresponds to an energy dissipation of about 18.8% in each vibrational load cycle. The highest peak temperature (~800 K) attained so far renders the current interstitial-alloyed HEAs suited for high-temperature damping applications. The current findings have important implications not only for developing advanced damping materials but also for broadening the application range of HEAs.

MATERIALS AND METHODS

Material preparation

Alloy ingots with a nominal composition of Ta0.5Nb0.5HfZrTi, $(Ta0.5Nb0.5HfZrTi)_{98}O_2$, and $(Ta0.5Nb0.5HfZrTi)_{98}N_2$ (at %) were prepared by arc-melting a mixture of pure metals (purity, >99.9 weight %), TiN (99.9 weight %), and TiO_2 (99.9 weight %) in a Ti-gettered high-purity argon atmosphere. The ingots were remelted at least eight times to ensure chemical homogeneity. Melted alloys were eventually drop-cast into a water-cooled copper mold with a dimension of 10 mm by 10 mm by 60 mm. Oxygen and nitrogen concentration in the samples was measured using a LECO Instruments inert gas fusion machine with infrared detection.

Internal-friction measurements

Beam-shaped samples with a dimension of 1 mm by 2 mm by 55 mm were used for damping-capacity measurement. The measurements were conducted on multifunction internal friction apparatus (MFP-1000) at low frequencies of 0.5, 1.0, 2.0, and 4.0 Hz over a temperature range from 300 to 1100 K with continuous heating in vacuum. All the testing samples were polished down to a 2000-grit SiC paper to eliminate surface scratches. A heating rate of 2 K min^{-1} and a forced vibration with the maximum strain amplitude of 2×10^{-4} were applied for the damping measurements, and experimental data were collected by an automated system (*54*). The background was subtracted according to the following equation

$$Q_b^{-1} = A + B\exp\left(\frac{-C}{k_B T}\right)$$

where Q_b^{-1} is the energy dissipation coefficient of the background, A, B, and C are the parameters to be determined after optimization of the χ^2 function, k_B is the Boltzmann constant, and T is the temperature (*29*).

Mechanical property measurements

Room temperature tensile properties were evaluated using a CMT4105 universal electronic tensile testing machine at the strain rate of 1×10^{-3} s^{-1}. Dog bone–shaped tensile samples with a section of 1.3 mm by 5 mm and a gauge length of 20 mm were cut by an electrical discharging machine.

Microstructural characterization

Phase identification of the as-cast alloys was conducted by XRD with Cu Kα radiation (MXP21VAHF). Microstructure was characterized by a Zeiss Supra 55 field emission scanning electron microscope equipped with an AZtecHKL EBSD (electron backscattering patterns) system. EBSD specimens were initially polished to 2000-grit SiC paper and subsequently electrochemically polished for the final surface clarification. The polishing was using a 6% perchloric acid + 30% *n*-butyl alcohol + 64% methyl alcohol solution with a direct voltage of 30 V at room temperature. An aberration-corrected FEI Titan G260-300 kV scanning transmission electron microscope was used to analyze the atomic structure of the as-cast samples. The TEM specimens were first mechanically ground to 50-μm thickness and then twin-jet electropolished using 6% perchloric acid + 30% *n*-butyl alcohol + 64% methyl alcohol solution. The specimens for the atom probe tomography measurements were prepared by focused ion beam milling on a dual-beam Helios 600. The CAMECA integrated visualization and analysis software IVAS 3.8.4 was used for data processing and three-dimensional atomic reconstruction.

SUPPLEMENTARY MATERIALS

Supplementary material for this article is available at http://advances.sciencemag.org/cgi/content/full/6/25/eaba7802/DC1

REFERENCES AND NOTES

1. I. Ritchie, Z.-L. Pan, High-damping metals and alloys. *Metall. Trans. A.* **22**, 607–616 (1991).
2. J. Wang, P. Song, S. Gao, X. Huang, Z. Shi, F. Pan, Effects of Zn on the microstructure, mechanical properties, and damping capacity of Mg-Zn-Y-Zr alloys. *Mater. Sci. Eng. A* **528**, 5914–5920 (2011).
3. X. Hu, Y. Zhang, M. Zheng, K. Wu, A study of damping capacities in pure Mg and Mg-Ni alloys. *Scr. Mater.* **52**, 1141–1145 (2005).
4. Y. Tanaka, Y. Himuro, R. Kainuma, Y. Sutou, T. Omori, K. Ishida, Ferrous polycrystalline shape-memory alloy showing huge superelasticity. *Science* **327**, 1488–1490 (2010).
5. A. Lai, Z. Du, C. L. Gan, C. A. Schuh, Shape memory and superelastic ceramics at small scales. *Science* **341**, 1505–1508 (2013).
6. J. San Juan, M. L. Nó, C. A. Schuh, Nanoscale shape-memory alloys for ultrahigh mechanical damping. *Nat. Nanotechnol.* **4**, 415–419 (2009).
7. I. Golovin, V. Palacheva, V. Y. Zadorozhnyy, J. Zhu, H. Jiang, J. Cifre, T. A. Lograsso, Influence of composition and heat treatment on damping and magnetostrictive properties of Fe-18%(Ga+Al) alloys. *Acta Mater.* **78**, 93–102 (2014).
8. T. Sakaguchi, F. Yin, Holding temperature dependent variation of damping capacity in a MnCuNiFe damping alloy. *Scr. Mater.* **54**, 241–246 (2006).
9. S. Laddha, D. C. Van Aken, H.-T. Lin, The effect of carbon on the loss of room-temperature damping capacity in copper-manganese alloys. *Metall. Mater. Trans. A* **28**, 105–112 (1997).
10. H. Watanabe, T. Sawada, Y. Sasakura, N. Ikeo, T. Mukai, Microyielding and damping capacity in magnesium. *Scr. Mater.* **87**, 1–4 (2014).
11. J. Snoek, Effect of small quantities of carbon and nitrogen on the elastic and plastic properties of iron. *Phys. Ther.* **8**, 711–733 (1941).
12. F. Yin, S. Iwasaki, D. Ping, K. Nagai, Snoek-type high-damping alloys realized in β-Ti alloys with high oxygen solid solution. *Adv. Mater.* **18**, 1541–1544 (2006).
13. H. Lu, C. Li, F. Yin, Q. Fang, O. Umezawa, Snoek-type damping behavior of surface oxidation-treated Ti-Mo alloys. *Mater. Sci. Eng. A* **528**, 3358–3366 (2011).
14. B. Cantor, I. T. H. Chang, P. Knight, A. J. B. Vincent, Microstructural development in equiatomic multicomponent alloys. *Mater. Sci. Eng. A* **375**, 213–218 (2004).
15. J. W. Yeh, S. K. Chen, S. J. Lin, J. Y. Gan, T. S. Chin, T. T. Shun, C. H. Tsau, S. Y. Chang, Nanostructured high-entropy alloys with multiple principal elements: novel alloy design concepts and outcomes. *Adv. Eng. Mater.* **6**, 299–303 (2004).
16. W. Guo, W. Dmowski, J.-Y. Noh, P. Rack, P. K. Liaw, T. Egami, Local atomic structure of a high-entropy alloy: An X-ray and neutron scattering study. *Metall. Mater. Trans. A* **44**, 1994–1997 (2012).
17. K.-Y. Tsai, M.-H. Tsai, J.-W. Yeh, Sluggish diffusion in Co-Cr-Fe-Mn-Ni high-entropy alloys. *Acta Mater.* **61**, 4887–4897 (2013).
18. Z. Li, C. C. Tasan, H. Springer, B. Gault, D. Raabe, Interstitial atoms enable joint twinning and transformation induced plasticity in strong and ductile high-entropy alloys. *Sci. Rep.* **7**, 40704 (2017).
19. M. Wang, Z. Li, D. Raabe, In-situ SEM observation of phase transformation and twinning mechanisms in an interstitial high-entropy alloy. *Acta Mater.* **147**, 236–246 (2018).
20. J. Su, D. Raabe, Z. Li, Hierarchical microstructure design to tune the mechanical behavior of an interstitial TRIP-TWIP high-entropy alloy. *Acta Mater.* **163**, 40–54 (2019).
21. Z. P. Lu, H. Wang, M. W. Chen, I. Baker, J. W. Yeh, C. T. Liu, T. G. Nieh, An assessment on the future development of high-entropy alloys: Summary from a recent workshop. *Intermetallics* **66**, 67–76 (2015).
22. Z. F. Lei, X. J. Liu, Y. Wu, H. Wang, S. H. Jiang, S. D. Wang, X. D. Hui, Y. D. Wu, B. Gault, P. Kontis, D. Raabe, L. Gu, Q. H. Zhang, H. W. Chen, H. T. Wang, J. B. Liu, K. An, Q. S. Zeng, T. G. Nieh, Z. P. Lu, Enhanced strength and ductility in a high-entropy alloy via ordered oxygen complexes. *Nature* **563**, 546–550 (2018).
23. O. Senkov, J. Scott, S. Senkova, D. Miracle, C. Woodward, Microstructure and room temperature properties of a high-entropy TaNbHfZrTi alloy. *J. Alloys Compd.* **509**, 6043–6048 (2011).
24. O. Senkov, J. Scott, S. Senkova, F. Meisenkothen, D. Miracle, C. Woodward, Microstructure and elevated temperature properties of a refractory TaNbHfZrTi alloy. *J. Mater. Sci.* **47**, 4062–4074 (2012).
25. S. Sheikh, S. Shafeie, Q. Hu, J. Ahlström, C. Persson, J. Veselý, J. Zýka, U. Klement, S. Guo, Alloy design for intrinsically ductile refractory high-entropy alloys. *J. Appl. Phys.* **120**, 164902 (2016).
26. H. Huang, Y. Wu, J. He, H. Wang, X. Liu, K. An, W. Wu, Z. Lu, Phase-transformation ductilization of brittle high-entropy alloys via metastability engineering. *Adv. Mater.* **29**, 1701678 (2017).
27. T. B. Massalski, H. Okamoto, P. Subramanian, L. Kacprzak, W. W. Scott, *Binary Alloy Phase Diagrams* (American Society for Metals,1986), vol. 1.

28. M. S. Blanter, I. S. Golovin, H. Neuhauser, H. Sinning, *Internal Friction in Metallic Materials: A Handbook*, 540 (2007).
29. A. S. Nowick, *Anelastic Relaxation in Crystalline Solids* (Elsevier, 2012), vol. 1.
30. S. Arrhenius, Über die Reaktionsgeschwindigkeit bei der Inversion von Rohrzucker durch Säuren. *Z. Phys. Chem.* **4**, 226–248 (1889).
31. R. Cantelli, Z. Szkopiak, Substitutional-interstitial interactions in niobium-titanium alloys: An internal friction study. *Appl. Phys.* **9**, 153–160 (1976).
32. F. Yin, L. Yu, D. Ping, Modeling and control of the high damping behavior in Ti-Nb-O alloys. *Mater. Sci. Eng. A* **521-522**, 372–375 (2009).
33. H. Lu, C. Li, F. Yin, Q. Fang, O. Umezawa, Effects of alloying elements on the Snoek-type relaxation in Ti-Nb-X-O alloys (X= Al, Sn, Cr, and Mn). *Mater. Sci. Eng. A* **541**, 28–32 (2012).
34. M. Weller, The Snoek relaxation in bcc metals-From steel wire to meteorites. *Mater. Sci. Eng. A* **442**, 21–30 (2006).
35. T. C. Niemeyer, C. R. Grandini, O. Florêncio, Stress-induced ordering due heavy interstitial atoms in Nb-0.3 wt.% Ti alloys. *Mater. Sci. Eng. A* **396**, 285–289 (2005).
36. L. Almeida, T. Niemeyer, K. Pires, C. R. Grandini, C. Pintão, O. Florêncio, Anelastic relaxation processes due oxygen in Nb-3.1 at.% Ti alloys. *Mater. Sci. Eng. A* **370**, 96–99 (2004).
37. C. R. Grandini, L. Ferreira, H. Sandim, O. Florêncio, H. Tejima, J. Jordão, Internal friction measurements in Nb-0.3 wt.% Ti containing oxygen. *Le Journal de Physique IV* **6**, C8-135-C138-138 (1996).
38. N. Kushnareva, S. Snejko, I. Yarosh, Internal friction in Nb-V-O alloys. *Acta Metall. Mater.* **43**, 4393–4401 (1995).
39. O. Florêncio, W. Botta, C. Grandini, H. Tejima, J. A. R. Jordao, Anelastic behaviour in Nb-Ti alloys containing interstitial elements. *J. Alloys Compd.* **211-212**, 37–40 (1994).
40. Z. Zhou, J. Xiong, S. Gu, D. Yang, Y. Yan, J. Du, Anelastic relaxation caused by interstitial atoms in β-type sintered Ti-Nb alloys. *J. Alloys Compd.* **509**, 7356–7360 (2011).
41. L. Almeida, C. R. Grandini, R. Caram, Anelastic spectroscopy in a Ti alloy used as biomaterial. *Mater. Sci. Eng. A* **521**, 59–62 (2009).
42. R. A. Nogueira, C. R. Grandini, A. P. R. A. Claro, Oxygen diffusion in Ti-10Mo alloys measured by mechanical spectroscopy. *J. Mater. Sci.* **43**, 5977–5981 (2008).
43. H. Y. Kim, S. Hashimoto, J. I. Kim, H. Hosoda, S. Miyazaki, Mechanical properties and shape memory behavior of Ti-Nb alloys. *Mater. Trans.* **45**, 2443–2448 (2004).
44. V. Khonik, L. Spivak, On the nature of low temperature internal friction peaks in metallic glasses. *Acta Mater.* **44**, 367–381 (1996).
45. H. Mizubayashi, Y. Ishikawa, H. Tanimoto, Study of hydrogenated amorphous alloys as high-strength and high-damping materials. *J. Alloys Compd.* **355**, 31–36 (2003).
46. M. Hasegawa, S. Yamaura, H. Kato, K. Amiya, N. Nishiyama, A. Inoue, Damping properties of hydrogen-absorbed rod metallic glasses. *J. Alloys Compd.* **355**, 37–41 (2003).
47. Y. Hiki, T. Yagi, T. Aida, S. Takeuchi, Low-frequency high-temperature internal friction of bulk metallic glasses. *J. Alloys Compd.* **355**, 42–46 (2003).
48. H. Mizubayashi, S. Murayama, H. Tanimoto, Feasibility study of high-strength and high-damping materials by means of hydrogen internal friction in amorphous alloys. *J. Alloys Compd.* **330**, 389–392 (2002).
49. S. Pennycook, B. Rafferty, P. Nellist, Z-contrast imaging in an aberration-corrected scanning transmission electron microscope. *Microsc. Microanal.* **6**, 343–352 (2000).
50. E. P. George, D. Raabe, R. O. Ritchie, High-entropy alloys. *Nat. Rev. Mater.* **4**, 515–534 (2019).
51. Y.-T. Shao, R. Yuan, Y. Hu, Q. Yang, J.-M. Zuo, The paracrystalline nature of lattice distortion in a high entropy alloy. arXiv:1903.04082 (2019).
52. I. S. Golovin, Damping mechanisms in high damping materials. *Key Eng. Mater.* **319**, 225–230 (2006).
53. N. Igata, K. Nishiyama, K. Ota, Y. Yin, W. Wuttig, I. S. Golovin, J. V. Humbeeck, J. San Juan, Panel discussion on the application of HDM. *J. Alloys Compd.* **355**, 230–240 (2003).
54. C. R. Grandini, A low cost automatic system for anelastic relaxations measurements. *Rev. Bras. Apl. Vácuo* **21**, 13–16 (2008).

Acknowledgments: We would like to dedicate this paper to the frontline medical personnel who are fighting the COVID-19 virus. We thank H. Zhao and W. Ye at the Max-Planck-Institut für Eisenforschung for help with APT analysis. **Funding:** This research was supported by the National Natural Science Foundation of China (nos. 51921001, 51871016, 51971017, 51531001, and 51671021), 111 Project (B07003), Program for Changjiang Scholars and Innovative Research Team in University of China (IRT-14R05), and the Projects of SKLAMM-USTB (2016Z-04, 2016-09, and 2016Z-16). Y.W. acknowledges the financial support from the Top-Notch Young Talents Program and Fundamental Research Fund for the Central Universities (no. FRF-TP-15-004C1). Z.Le. thank the Max-Planck-Gesellschaft for a fellowship. Z.Lu, Z.Le., and Y.W.: Chinese patent: Development and fabrication of high-temperature high-damping high-entropy alloys. Application no.: CN20111319204.6. File date: 7 November 2018. Proclamation no.: CN109338200A. Date: 15 February 2019. Inventors: Z.Lu, Z.Le., Y.W., H.W., and X.L. Category: C22C30/00. Affiliation: University of Science and Technology Beijing. **Author contributions:** Z.Lu designed the study. Z.Le. carried out the main experiments. Z.Le., B.G., D.R., and Z.Lu analyzed the data and wrote the main draft of the paper. L.G. and Q.Z. conducted the STEM characterizations. B.G., J.H., and Z.Le. prepared the atom probe tomography specimens, processed the data, and interpreted the results. All authors contributed to the discussion of the results and commented on the manuscript. **Competing interests:** The authors declare that they have no competing interests. **Data and materials availability:** All data needed to evaluate the conclusions in the paper are present in the paper and/or the Supplementary Materials. Additional data related to this paper may be requested from the authors.

Submitted 8 January 2020
Accepted 5 May 2020
Published 17 June 2020
10.1126/sciadv.aba7802

Citation: Z. Lei, Y. Wu, J. He, X. Liu, H. Wang, S. Jiang, L. Gu, Q. Zhang, B. Gault, D. Raabe, Z. Lu, Snoek-type damping performance in strong and ductile high-entropy alloys. *Sci. Adv.* **6**, eaba7802 (2020).